

Constraining the rotation profile in a low-luminosity subgiant with a surface rotation measurement

Tanner A. Wilson^{1,2,★}, Andrew R. Casey^{1,2}, Ilya Mandel^{1,3}, Warrick H. Ball⁴, Earl P. Bellinger^{5,6} and Guy Davies^{4,6}

¹*School of Physics & Astronomy, Monash University, Victoria, 3800, Australia*

²*Center of Excellence for Astrophysics in Three Dimensions (ASTRO-3D), Australia*

³*The ARC Center of Excellence for Gravitational Wave Discovery – OzGrav, Australia*

⁴*School of Physics and Astronomy, University of Birmingham, Edgbaston, B15 2TT, UK*

⁵*Max Planck Institute for Astrophysics, Garching, 85748, Germany*

⁶*Stellar Astrophysics Centre (SAC), Department of Physics and Astronomy, Aarhus University, Aarhus C, DK-8000, Denmark*

Accepted 2023 March 10. Received 2023 March 7; in original form 2023 February 3

ABSTRACT

Rotationally induced mode splitting frequencies of low-luminosity subgiants suggest that angular momentum transport mechanisms are 1–2 orders of magnitude more efficient in these stars than predicted by theory. Constraints on the rotation profile of low-luminosity subgiants could be used to identify the dominant mechanism for angular momentum transport. We develop a forward model for the rotation profile given observed rotational splittings, assuming a step-like rotation profile. We identify a consistent degeneracy between the position of the profile discontinuity and the surface rotation rate. We perform mock experiments that show the discontinuity position can be better constrained with a prior on the surface rotation rate, which is informed by star spot modulations. We finally apply this approach to KIC 12508433, a well-studied low-luminosity subgiant, as an example case. With the observed surface rotation prior, we obtain a factor of 2 increase in precision of the position of strong rotation gradient. We recover the literature values of the core and surface rotation rates and find the highest support for a discontinuity in the radiative zone. Auxiliary measurements of surface rotation could substantially improve inferences on the rotation profile of low-luminosity subgiants with already available data.

Key words: asteroseismology – stars: rotation.

1 INTRODUCTION

All stars rotate. The rotation rate and distribution of angular momentum throughout a star evolves with time. The effects of rotation on the structure and evolution of a star are substantial (e.g. Heger 1998; Maeder & Meynet 2000), and accurate prescriptions of rotation in stellar models are important to reproduce observations, particularly asteroseismic measurements of oscillation modes.

Low-mass subgiants and low-luminosity red giants pulsate in mixed modes, which are sensitive to structure in both the core and envelope. Mixed modes result from the near-surface convection, which drives the oscillation modes to amplitudes that are detectable in space-based photometry missions like *CoRoT* (Baglin 2003) and *Kepler* (Borucki et al. 2010). Rotation lifts the degeneracy of oscillation modes of the same angular degree and azimuthal order. The change to the frequency of rotationally split modes is related to the rotation profile. For this reason, measuring rotational splittings allows us to constrain the rotation profile.

Current measurements of rotational splittings place low precision constraints on the core and surface rotation rates [≈ 10 per cent and 30 per cent, respectively (e.g. Deheuvels et al. 2014; Felling et al.

2021)] and have little capability to constrain the shape of the rotation profile connecting the core and the surface. These observations, however, present some notable results. Subgiants demonstrate solid-body rotation early in their transition off the main-sequence (MS), like their MS counterparts (Deheuvels et al. 2020; Noll, Deheuvels & Ballot 2021). However, later in their post-MS evolution, the cores of more evolved subgiants and low-luminosity red giant branch (RGB) stars rotate much faster than their envelope. The core-to-surface rotation ratio can grow to ≈ 20 for stars leaving the subgiant phase (Deheuvels et al. 2014; Gehan et al. 2018; Eggenberger et al. 2019).

Stellar models predict differential rotation between the core and the surface to be two to three orders of magnitude greater than observations suggest (Eggenberger, Montalbán & Miglio 2012; Cantiello et al. 2014). The surface rotation rates of white dwarfs agree well with the core rotation rates of RGB stars (Gough 2015; Hermes et al. 2017), suggesting an angular momentum transport mechanism that is much more efficient throughout the first ascent of the RGB, and nowhere else (Eggenberger et al. 2012; Ceillier et al. 2013; Marques et al. 2013; Fuller et al. 2015; Spada et al. 2016; Ouazzani et al. 2018).

The angular momentum transport mechanism sets the rotation profile. The core-to-surface rotation ratio and the position and strength of the gradient of rotation rate can characterize the rotation profile. Felling et al. (2021) suggest that tighter constraints can be

* E-mail: tanner.wilson@monash.edu

made on angular momentum transport mechanisms through more precise measures of the core-to-surface rotation ratios of post-MS stars (Deheuvels et al. 2014), and of the position and strength of a rotation rate gradient (Di Mauro et al. 2018). For example, a rotation profile with a constant rotation rate internal to the base of the convective zone (BCZ), and a decreased rotation rate that is inversely dependent on radius in the BCZ, could be indicative of angular momentum transport from deep fossil magnetic fields (Gough & Thompson 1990; Kissin & Thompson 2015; Takahashi & Langer 2021). This results from differential rotation being damped along poloidal field lines (Garaud 2002; Strugarek, Brun & Zahn 2011). On the other hand, a steep rotational gradient near the H-burning shell of a subgiant would indicate turbulent angular momentum transport. This could be in the form of internal gravity waves (Pinçon et al. 2017), leading to localized shallow gradients in the profile (Charbonnel & Talon 2005) or through magneto-rotational instabilities that arise from steep angular momentum gradients (Balbus & Hawley 1994; Arlt, Hollerbach & Rüdiger 2003; Menou & Mer 2006; Spada et al. 2016). The gradient of the rotation profile of subgiants is not well constrained through current asteroseismic data (Deheuvels et al. 2014).

In this work, we consider the constraints to the position of a steep rotational gradient, where we show that $\ell = 1, 2$ rotational splittings may be sufficient to make valuable inferences about the rotation profiles of low-luminosity subgiants if a precise auxiliary measure of surface rotation rate is available. We specifically investigate the impact of employing surface rotation periods from photometric variability owing to stellar spots (e.g. those measured in Garcia et al. 2014; McQuillan, Mazeh & Aigrain 2014; Santos et al. 2021). In adopting these values, we utilize a data set that overlaps with the subset used to measure asteroseismic rotational splittings. We deem it appropriate to employ both constraints simultaneously due to the distinct methods of measuring these quantities.

In Section 2, we describe a forward model to infer rotation profile parameters given observed rotational splittings, assuming a step rotation profile. We perform tests using mock data generated by three hypothetical profiles to show the differences in constraining the rotation profile with realistic independent measures of surface rotation rate from stellar spot brightness modulations. Finally, we perform inference on the observed rotational splittings of KIC 12508433 with different priors and compare the constraints on the rotation profile. The implications are discussed in Section 4 and summarized in Section 5.

2 METHOD AND RESULTS

2.1 Rotational splittings

Stellar oscillations can be decomposed into oscillating spherical harmonic modes. Individual modes frequencies ($\nu_{n,\ell,m}$) are characterized by their radial order (n), angular degree (ℓ), and azimuthal order (m). Low-luminosity subgiants have much longer rotation periods [of order 10^1 d (Deheuvels et al. 2014)] in the fast rotating core than the average oscillation period (on the order of hours; Aerts, Christensen-Dalsgaard & Kurtz 2010). We can therefore treat rotation as perturbative to the structure. The effect of stellar rotation on oscillation mode frequencies can be approximated as perturbations to the non-rotating mode frequencies from $m = 0$ to $m = -\ell$ and $m = \ell$. This is a widely employed approximation in the field of asteroseismic inversions of rotation (e.g. Deheuvels et al. 2014, 2015; Fellay et al. 2021). For more detail on this approach,

see Unno et al. (1989) and Aerts et al. (2010). To first order, the rotationally split oscillation frequencies are

$$\nu_{n,\ell,m} = \nu_{n,\ell,0} + \delta\nu_{n,\ell,m} \quad (1)$$

$$= \nu_{n,\ell,0} + m \delta\nu_{n,\ell}, \quad (2)$$

where $\nu_{n,\ell,m}$ is the frequency of the n, ℓ, m mode, $\nu_{n,\ell,0}$ is the frequency in the non-rotating case, and $\delta\nu_{n,\ell,m}$ is the change in oscillation frequency due to rotation, known as the rotational splitting. The difference between the $m = 0$ and $m \neq 0$ mode frequency is the m th multiple of the $\delta\nu_{n,\ell}$ rotational splitting. In practice, we are usually only able to observe $\ell = 1$ and $\ell = 2$ modes with $m = 1$ and $m = -1$ rotational splittings in low-luminosity subgiants from photometric time series data (Benomar et al. 2013; Deheuvels et al. 2014).

Rotational splittings are scaled averages of the rotation profile. The scaling is different for each oscillation mode and is quantified using a so-called rotational kernel. The rotational kernels are inherent to the thermodynamic structure of a star (see Aerts et al. 2010 for a derivation of these kernels). Assuming spherical symmetry, the n, ℓ rotational splitting is given by

$$\delta\nu_{n,\ell}(\Omega) = \beta_{n,\ell} \int_0^R K_{n,\ell}(r) \Omega(r) dr, \quad (3)$$

where $K_{n,\ell}$ is the rotational kernel of the n, ℓ mode (determined from a stellar model), $\Omega(r)$ is the scaled average, with respect to the polar axis, 1D rotation profile along the radial axis, $\beta_{n,\ell}$ is a normalization constant, and R is the outermost radius of the star. The rotational kernel, and thus scaled averaged frequency shift, changes with each oscillation mode. Changes to the rotation profile therefore result in distinct variances for each rotational splitting. Some rotation profiles are more likely to result in measurable rotational splittings than others. As a result we are able to use forward modelling to determine the set of likely rotation profiles given some observed rotational splittings.

2.2 Forward model

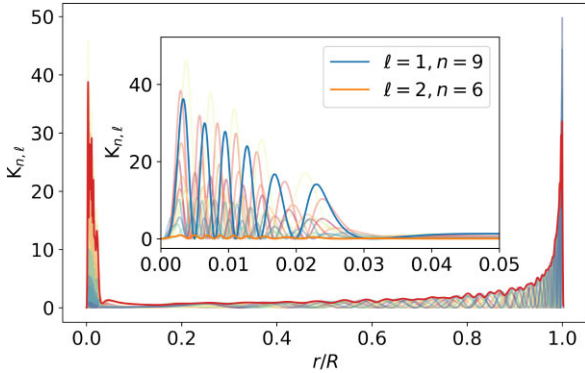
A forward model requires a set of rotation kernels to predict rotational splittings given some profile. In this work, we use rotational kernels of the low-luminosity subgiant KIC 12508433, a well-studied asteroseismic target (e.g. Deheuvels et al. 2014). Models of KIC 12508433 indicate that it is early in its evolution off the MS, which is supported by a relatively low core-to-surface rotation ratio. It is the earliest star known in its post-MS evolution with evidence of differential rotation.

We were provided with a model of KIC 12508433 from Ball & Gizon (2017) generated using the ASTERO module of the Modules for Experiments in Stellar Astrophysics (MESA) evolutionary code (r7624; Paxton et al. 2010, 2013, 2015, 2019). The model was found by simultaneously matching the non-seismic properties of KIC 12508433 (T_{eff} , $\log g$, and $[\text{Fe}/\text{H}]$ in Table 1), the global seismic quantities – the frequency where peak power of the Gaussian asteroseismic power envelope occurs, ν_{max} , and the frequency spacing between consecutive radial order modes with the same angular degree, $\Delta\nu$ – and the observed mode frequencies (see tables 1 and 3 in Deheuvels et al. 2014) to those predicted by the model. Mode frequencies were calculated using ADIPLS (Christensen-Dalsgaard 2008), with combined surface effect corrections to the frequencies (Ball & Gizon 2014, 2017).

Most of the observed and best-fit model quantities agree to within 1σ . The exceptions are T_{eff} and L where the agreement is within

Table 1. Measured properties of KIC 12508433 (Deheuvels et al. 2014), and those of the best-fitting stellar model from which the rotation kernels are generated.

	KIC 12508433	Model
$M (M_\odot)$	1.20 ± 0.16	1.293
$R (R_\odot)$	2.20 ± 0.10	2.277
$L (L_\odot)$	3.25 ± 0.45	4.065
$\log g \text{ (cm s}^{-2}\text{)}$	3.83 ± 0.04	3.834
$T_{\text{eff, spec}} \text{ (K)}$	5248 ± 130	5434
$[\text{Fe}/\text{H}] \text{ (dex)}$	0.25 ± 0.23	0.06

**Figure 1.** Rotational kernels for the best-fitting model of KIC 12508433. The red curve shows three times the local standard deviation of the set of observed kernels (kernel deviation). Regions with large kernel deviation are expected to be sensitive to the rotation profile following forward modelling. In this model, these regions can be seen in the H-burning shell core ($r/R < 0.05$) and nearing the surface ($r/R > 0.8$). The inset shows the same kernels with two modes highlighted: the $\ell = 1, n = 9$ mode (blue) is sensitive to core rotation and the $\ell = 2, n = 6$ (orange) is sensitive to surface rotation.

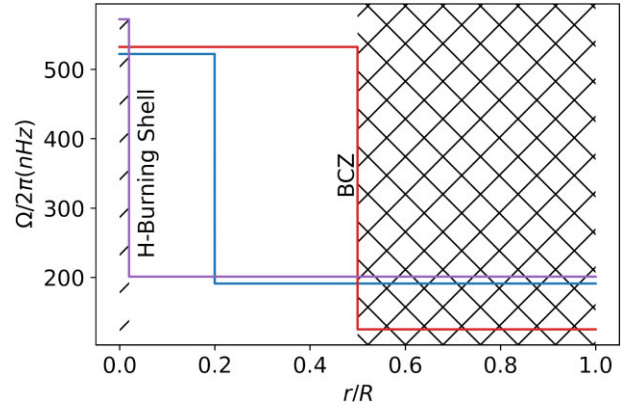
2σ . Our model T_{eff} is closer to the reported T_{eff} from the infrared flux method (Casagrande et al. 2010; 5302 ± 124 K from Deheuvels et al. 2014), but fully consistent with the spectroscopic effective temperature. L is not included in the χ^2 fitting of the model (M , R , and L are outputs of the model) and the value from Deheuvels et al. (2014) was estimated from scaling relations. This level of deviation varies with surface modelling assumptions (Ball & Gizon 2017), is consistent with previous works (e.g. Deheuvels et al. 2014; Li et al. 2020), and while rotational inversions of subgiants can be dependent on model uncertainties (Schunker, Schou & Ball 2016); this discrepancy is unlikely to affect the results of this work.

We used this model of KIC 12508433 to calculate the rotational kernels for all observable rotational splittings. Radial positions with both high kernel magnitude and inter-kernel variance (represented by the standard deviation of kernel magnitudes, shown in red in Fig. 1) are most sensitive to the rotation profile. For KIC 12508433, these regions are near the core and at $r/R > 0.8$.

Deheuvels et al. (2014) concluded that it is difficult to distinguish between smooth and discontinuous rotation profiles of low-luminosity subgiants using current data. Consequently, we assume a simple form of a rotation profile $\Omega(r)$ using three parameters of the following form:

$$\Omega(r) = \begin{cases} \Omega_c & r/R \leq p \\ \Omega_s & r/R > p \end{cases}, \quad (4)$$

where Ω_c and Ω_s describe the core and surface rotation rates, respectively, and p is the position of the step (in units of r/R). We

**Figure 2.** Three rotation profiles used in the mock data experiments. These profiles represent the extreme consequences of different angular momentum transport mechanisms in low-luminosity post-MS stars. Cross-hatching represents the convective surface region and diagonal-hatching represents the H-burning shell. See Section 3.1 for descriptions of each profile.

discuss the implications of the assumed step-function form of the rotation profile further in Section 4. Initially, we will assume weak uninformed, uniform priors on the core and surface rotation rate and a uniform prior on p :

$$p \sim \mathcal{U}(0, 1), \quad (5)$$

$$\Omega_s/2\pi \sim \mathcal{U}(0, 600) \text{ nHz}, \quad (6)$$

$$\Omega_c/2\pi \sim \mathcal{U}(0, 1000) \text{ nHz}, \quad (7)$$

where $\mathcal{U}(x, y)$ denotes a uniform prior between x and y . We calculate the expected rotational splitting frequencies $\delta\nu_{n,l}$ for all observable $\{n, l\}$ modes given a model $\Omega(r)$ and the rotational kernels $K_{n,l}(r)$ using equation (3), and assume the observed splitting frequencies are normally distributed with a log-likelihood

$$\ln \mathcal{L}(\delta\nu | \Omega_c, \Omega_s, p, \mathbf{K}(r), \sigma_{\delta\nu}) \propto -\frac{1}{2} \sum_{n,l} \left(\frac{\delta\nu_{n,l} - \delta\nu_{\text{obs } n,l}}{\sigma_{\delta\nu_{n,l}}} \right)^2, \quad (8)$$

where $\delta\nu_{\text{obs } n,l}$ is the observed rotational splitting frequency for mode n and l , and its associated uncertainty is $\sigma_{\delta\nu_{n,l}}$. The vector-valued symbols $\delta\nu$, $\mathbf{K}(r)$, and $\sigma_{\delta\nu}$ indicate that the log-likelihood depends on the corresponding values for all of the observed rotational splittings. We constructed this model using PyMC3 (Salvatier, Wiecki & Fonnesbeck 2016) and used the ‘No U-Turn Sampler’ (Hoffman & Gelman 2011) to draw samples from the posterior.

3 RESULTS

3.1 Mock data experiments with three hypothetical rotation profiles

We begin by generating mock data with our forward model to test the impact of independent measures of surface rotation rate. We chose three rotation profiles with extreme differences in the position of a strong rotational gradient, which represent hypothetical angular momentum transport mechanisms that could result in step-like rotation profiles. The three step positions are: in the H-burning shell (purple); in the radiative zone (blue); and at the base of the BCZ (red) as shown in Fig. 2. The mock rotation profiles are motivated by, but not representative of, various angular momentum transport

processes. The BCZ step rotation profile (red) is a signature of angular momentum transport by fossil magnetic fields, which results in solid body rotation in the radiative region and inverse rotation rate on radius in the convective region (Kissin & Thompson 2015; Takahashi & Langer 2021). The H-burning step rotation profile (purple) is indicative of turbulent angular momentum transport through internal gravity waves (Pinçon et al. 2017) or magnetorotational instabilities (Balbus & Hawley 1994; Arlt et al. 2003; Menou & Mer 2006; Spada et al. 2016) which result in a strong gradient in rotation rate close to the core. The radiative zone step profile (blue) corresponds to delocalized angular momentum transport from the core into the radiative zone and is not indicative of a specific angular momentum transport process.

The core and surface rotation rates will be realistically different for each profile/angular momentum transport process. To account for this for each profile, we fixed the step position and evaluated the log-likelihood (given the observed splittings of KIC 12508433) at each combination of (Ω_c , Ω_s) and set the rotation rates to those with the maximum log-likelihood. The resulting rotation profiles are shown in Fig. 2: radiative-zone step (blue: $p = 0.2$), a BCZ step (red: $p = 0.5$), and the H-burning shell step (purple: $p = 0.05$). The rotational splitting frequencies of these profiles were then calculated using (equation 3). We adopted uncertainties on those expected values given the precision of mode frequencies measured in KIC 12508433 (table 3 of Deheuvels et al. 2014). This provides us with three mock data sets to consider the rotation profile's effect on the observations.

We treated the mock data generated by each step profile as if it were real data and performed inference using the model and sampler described in Section 2.2. We performed inference twice: first with a flat prior on surface rotation and then with a Gaussian prior on surface rotation with mean equal to the injected surface rotation rate, and a standard deviation 10 per cent of the mean value. Here, we have chosen 10 per cent as representative of the average uncertainty on state-of-the-art measurements of MS and subgiant stellar rotation from photometric variation (Santos et al. 2021). We discuss this choice further in Section 4. We drew 20 000 posterior samples in each case. The 1D marginalized posterior samples with a flat and informed prior are compared in Fig. 3. The full posteriors are shown in the Appendix (Figs A1–A6).

When sampling with a uniform prior on surface rotation (Figs A1–A3), we identify multi-modality and a strong correlation between Ω_s and p : smaller Ω_s values tend to coincide with higher p values. The inferred step position p is very uncertain in all three cases, showing nearly uniform probability throughout the domain.

The impact of an auxiliary surface rotation rate measure on the posterior distributions is evident when comparing the normalized posterior density when using an uninformed prior (thin dashed) to the informed prior (thick solid) in Fig. 3. When the informed prior is introduced, the degeneracy between surface rotation rate and p is broken and the surface rotation rate and p are better recovered. In the H Shell step (purple) and radiative step (blue) experiments, the prior has collapsed support for $p > 0.4$. The introduction of the prior does not, however, allow us to differentiate between rotation profiles deeper in the star. We find that for profiles where $p \lesssim 0.2$, multimodality remains and the introduction of the prior on Ω_s increased support for p closer to the core (and closer to the true value). Indeed, the introduction of the informed prior for the H shell and radiative step experiments has constrained the posterior on p , but the 1σ range on these values overlaps significantly. We could not differentiate between these profiles using this method and state-of-the-art data. This is not the case for the BCZ mock data experiment. Introducing the informed surface rotation prior allows us to place

more significant constraints on p . The posterior on p was flat with an uninformed prior and the BCZ step. In contrast, with a surface rotation rate prior, the posterior is now a single peak centred at the injected value with a percentage standard deviation of the median value of about 18 per cent. This illustrates the constraining power on p of the independent measures of Ω_s in specific circumstances.

3.2 KIC 12508433

Our mock data experiments confirm that a realistic measure of surface rotation rate, treated as a prior during inference can better constrain the internal rotation profile. We now apply this method to observed rotational splittings of KIC 12508433 (Deheuvels et al. 2014). First with a uniform prior on surface rotation between 0 and 600 nHz, and then with an independent surface rotation rate (measured by Garcia et al. 2014, from photometry) treated as a Gaussian prior on the surface rotation rate with mean 172 nHz and standard deviation 21 nHz. The posteriors are shown in Figs 4 and 5. The best-fitting values and credible intervals of the rotation profile parameters for each prior are shown in Table 2 and are compared to the results of optimally localized average (OLA) inversions performed in Deheuvels et al. (2014).

With a uniform prior, the median of the posterior on the core and surface rotation rates and corresponding 16th and 84th percentile credible intervals are $\Omega_c/2\pi = 524^{+36}_{-34}$ nHz and $\Omega_s/2\pi = 141^{+51}_{-79}$ nHz, with the maximum a posteriori or MAP point at $\Omega_c/2\pi \approx 520$ nHz and $\Omega_s/2\pi \approx 170$ nHz. With the informed surface rotation rate prior the 16th and 84th percentile credible intervals are $\Omega_c/2\pi = 525^{+39}_{-35}$ nHz and $\Omega_s/2\pi = 175^{+19}_{-21}$ nHz. The inferences agree with each other, as well as the inversions performed in Deheuvels et al. (2014). Those authors use OLA to estimate the mean rotation rate in the g-mode cavity to be $\langle\Omega_g\rangle/2\pi = 532 \pm 79$ nHz and the mean rotation rate in the p-mode cavity to be $\langle\Omega_p\rangle/2\pi = 213 \pm 26$ nHz. Taking their Ω_g and Ω_p as analogues for Ω_c and Ω_s , respectively, both sets of quantities agree within about one joint standard deviation, without considering that the *mode* of the Ω_s posteriors are closer to $\langle\Omega_p\rangle$ than the median of Ω_s .

Like in the mock data experiments, the independent surface rotation measure removed support for discontinuities close to the BCZ (comparing Figs 4 and 5), but two peaks remain: $p \approx 0.25$ (closest to the median posterior value and a peak in the posterior when considering a flat prior on Ω_s) and a much smaller peak closer to the core. Rotation profiles with a discontinuity located $p > 0.4$ for KIC 12508433 is strongly disfavoured, and a discontinuity in the radiative region $0.2 r/R$ is favoured. Comparing the confidence intervals when applying a flat and informed prior, we obtain a factor of approximately two increase in measurement accuracy on p .

4 DISCUSSION

We find that a surface rotation rate measured from star spot modulations can substantially improve inferences on the rotation profiles of low-luminosity subgiants. This takes advantage of a degeneracy between Ω_s and p , found by performing inference using mock experiments with different discontinuity positions.

Including an independent measure of surface rotation as a prior in the analysis of KIC 12508433 yields increased support for step-like profiles with rotational gradients in the radiative zone and decreased support for step-like rotation profiles with $p \gtrsim 0.4$.

In our mock data tests, we proposed that a step-like rotation profile with a rotational gradient at $0.5 r/R$ (BCZ profile) is motivated by, but not representative of, angular momentum transport by fossil

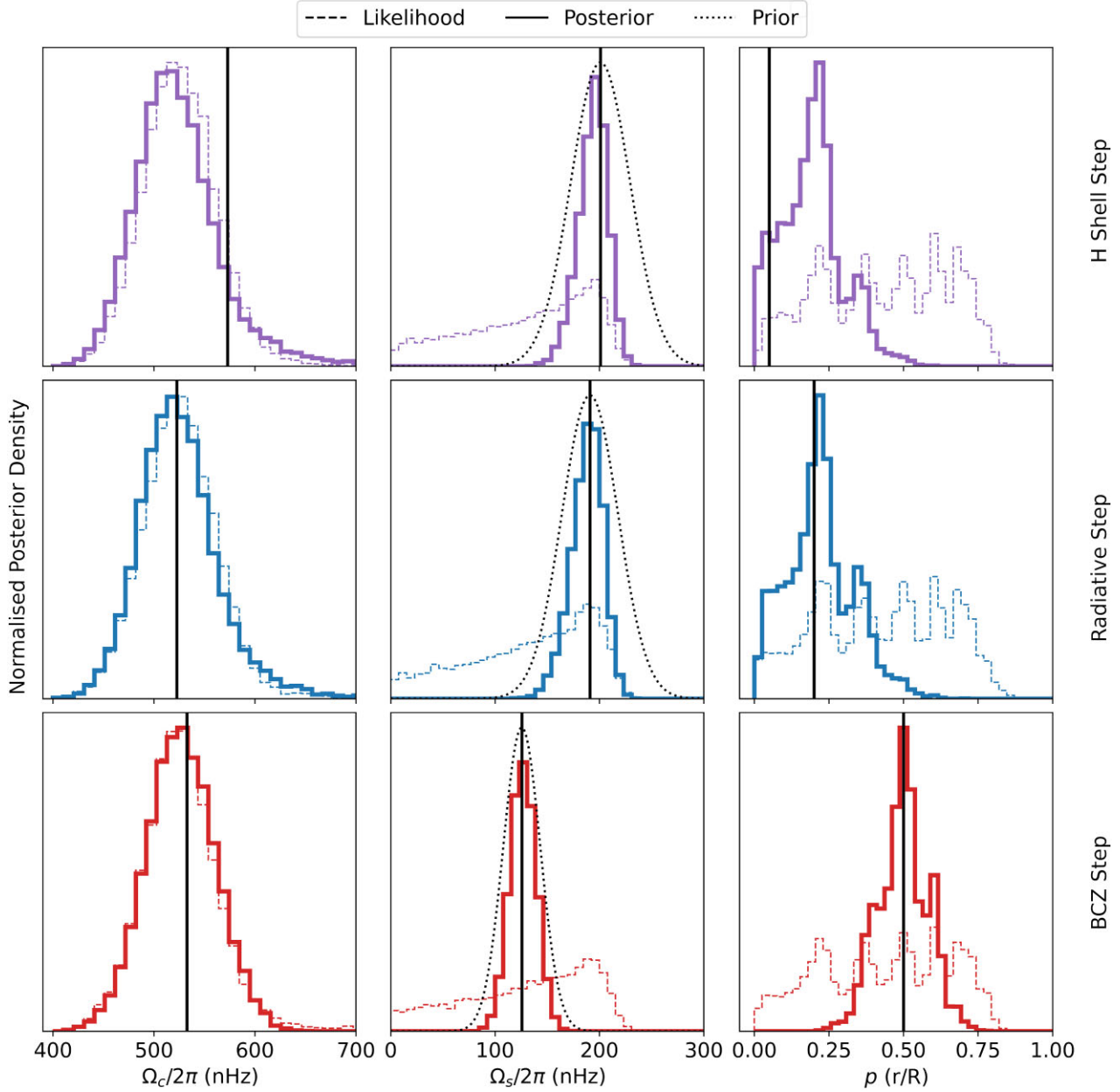


Figure 3. Normalized posterior density following sampling for each *mock* rotational splitting experiment. From left to right, the normalized posterior density of each of the parameters of the rotation profile model are shown: surface rotation rate ($\Omega_s/2\pi$), core rotation rate ($\Omega_c/2\pi$), and position of rotational gradient (p). Thin coloured dashed lines are samples with no prior on the surface rotation rate, thin dotted black lines correspond to the introduced prior on surface rotation rate, and thick coloured lines correspond to samples when the informed surface rotation prior was introduced. Vertical black lines correspond to the input values for each of the rotation profile parameters used to generate the mock rotational splittings. From top to bottom, each row displays the result of sampling a different set of rotational splittings with the same colours as the rotation profiles used to generate the mock data in Fig. 2: the H-burning shell step (purple), radiative zone step (blue), and base of BCZ step (red).

magnetic fields. However, the simplified step rotation profile does not accurately recreate the inverse dependency of rotation rate with radius beyond the BCZ indicative of this angular momentum transport process. Further, the signature rotation profile becomes most apparent in the red giant branch (Fellay et al. 2021; Takahashi & Langer 2021). Therefore, we are not proposing a lack of support for eliminating fossil magnetic fields as a possible explanation for the subgiant angular momentum transport problem.

The auxiliary measure of surface rotation we adopt as a surface rotation rate prior requires some discussion. The ‘data’ we use are

rotational splitting frequencies measured from a Fourier transform of a photometric time series. The measured surface rotation rate from Garcia et al. (2014) also uses some subset of the same photometric time series data. The two sets of measurements are not strictly statistically independent, such that there is a risk that we are ‘stealing information’. The two approaches do use subsets of the same data set, but the methods are sufficiently distinct that we consider it reasonable to use the surface rotation rate here.

Santos et al. (2021) suggest that the average percentage uncertainty on photometric surface rotation measurements is ~ 10 per cent

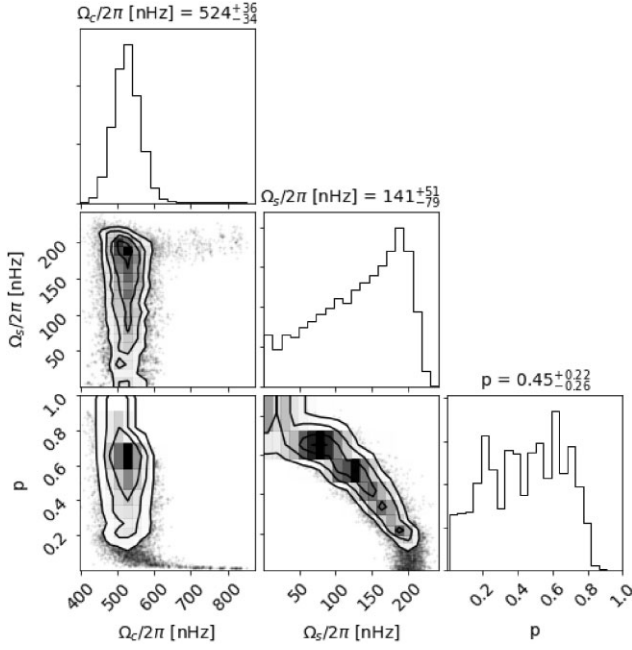


Figure 4. Posterior distributions of the core rotation rate Ω_c , the surface rotation rate Ω_s , and the discontinuity position p (equation 4) given the observed $l = \{1, 2\}$ rotational splittings of KIC 12508433 and assuming a rotation profile with a step function.

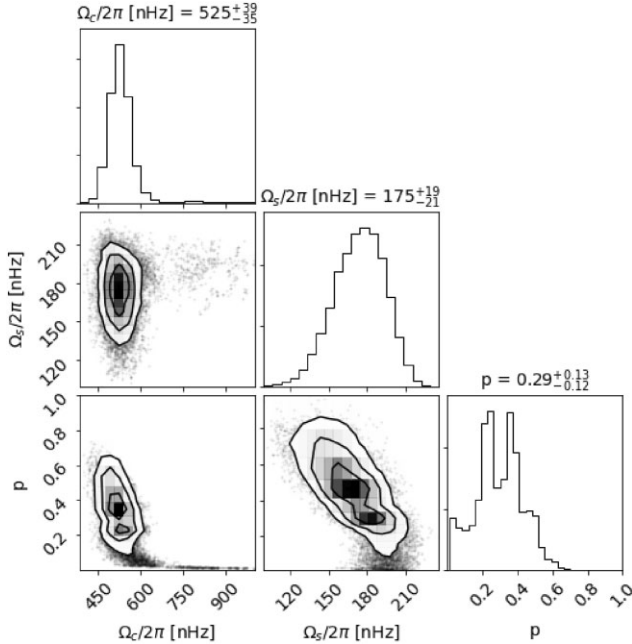


Figure 5. Posteriors on step profile parameters given the rotational splittings of KIC 12508433 and informed prior on surface rotation rate from (Garcia et al. 2014).

for MS and subgiant stars. The precision varies with temperature, and peaks around 6000 K (the Kraft break). Those authors also concluded that only about 20 per cent of subgiants with long and precise photometric observations from *Kepler* have measurable rotation periods. Subgiants may express smaller, shorter-lived active regions, which, when combined with long rotation periods, would present a smaller observable fraction and less precise measures of

Table 2. Best-fitting rotation profile parameters given observed $\ell = 1$ and 2 rotational splittings of KIC 12508433 from optimally localized averages (OLA; Deheuvels et al. 2014) and forward modelling with flat and informed ($\Omega_s/2\pi = 172 \pm 21$ nHz) priors. OLA does not place constraints on the rotation profile outside the g- and p-mode cavities in the core and at the star’s surface, respectively. p is more precisely measured with the introduction of the informed prior when forward modelling.

	$\Omega_c/2\pi$ (nHz)	$\Omega_s/2\pi$ (nHz)	p (r/R)
Deheuvels et al. (2014) (OLA)	532 ± 79	213 ± 26	–
Sampling – flat Ω_s Prior	524^{+36}_{-34}	141^{+51}_{-79}	$0.45^{+0.22}_{-0.26}$
Sampling – informed Ω_s Prior	525^{+39}_{-35}	175^{+19}_{-21}	$0.29^{+0.13}_{-0.12}$

the surface rotation rate when compared to MS counterparts. On the other hand, observing rotational splittings in subgiants requires a long observation time, which may lend itself to a higher fraction with measurable surface rotation rates.

It’s difficult to precisely measure the surface rotation rate without using photometry. Rotational velocity ($v \sin i$) only requires a single high-resolution spectrum, but requires an estimate of the inclination angle and the star’s radius, which is quickly changing in the post-MS and is strongly model dependent.

We assumed a step-like (discontinuous) function for the rotation profile, consistent with other works (e.g. Fellay et al. 2021). Realistically, this may not reflect the true shape of the rotation profile of any low-luminosity subgiant. Asteroseismic forward modelling of the stellar rotation profile is an ill-posed problem. The observed rotational splittings alone do not uniquely determine the shape of a star’s rotation profile. An assumption of the rotation profile’s shape is necessary for the rotational splittings to constrain the range of possible rotation profile parameters. A much more flexible model than the step-like rotation profile could be employed. However, the inferences must be interpreted in the context of the realistic evolution of angular momentum transport. Ultimately, our work exemplifies that introducing an informed surface rotation prior further reduces the potential rotation profiles already constrained by asteroseismic data. Combining state-of-the-art asteroseismic and surface rotation data is a practical method to obtain more substantial constraints to the evolution of rotation from already available data.

In this work, we take KIC 12508433 as an example of a low-luminosity giant with asteroseismic observations. It is not yet clear whether the degeneracy between surface rotation and step position generalises across all subgiants of different masses, metallicities, and ages. Very few subgiants are known to have mode measurements suitable for this kind of inference. Further work is needed.

5 CONCLUSIONS

We investigate the impact of independent surface rotation rate priors on inference of the rotation profile of subgiant stars. We perform forward modelling of the rotation profile given observations of rotational splittings assuming a step function rotation profile. Under these assumptions, we identify a degeneracy between the surface rotation rate and the position of the strong gradient. Mock experiments show that the introduction of a prior on surface rotation breaks the degeneracy, allowing us to place stronger constraints on the position of the gradient.

We introduce an independent measure of surface rotation from star spot photometric modulations as a prior when performing inference on the rotation profile of KIC 12508433. We find that introducing the independent measure of surface rotation increases the measurement precision on the position of the rotational gradient by a factor of 2 and

that the data strongly disfavours discontinuities outside $r/R = 0.4$ in KIC 12508433. Including auxiliary surface rotation measurements when performing asteroseismic forward modelling of the rotation profile is a simple way of extending what we can learn from each star with existing data.

ACKNOWLEDGEMENTS

We thank the anonymous referee for their thorough review of this work and for their helpful suggestions. ARC is supported in part by the Australian Research Council through a Discovery Early Career Researcher Award (DE190100656). Parts of this research were supported by the Australian Research Council Centre of Excellence for All Sky Astrophysics in 3 Dimensions (ASTRO 3D), through project number CE170100013. IM acknowledges support from the Australian Research Council Centre of Excellence for Gravitational Wave Discovery (OzGrav), through project number CE17010004. IM is a recipient of the Australian Research Council Future Fellowship FT190100574. WHB thanks the UK Science and Technology Facilities Council (STFC) for support under grant ST/R0023297/1. This work has received funding from the European Research Council (ERC) under the European Union's Horizon 2020 research and innovation programme (CartographY GA 804752). Funding for the Stellar Astrophysics Centre is provided by The Danish National Research Foundation (grant agreement no. DNRF106).

DATA AVAILABILITY

The data and models underlying this article are available upon request to the corresponding author.

REFERENCES

- Aerts C., Christensen-Dalsgaard J., Kurtz D. W., 2010, *Asteroseismology*. Springer, Dordrecht
- Arlt R., Hollerbach R., Rüdiger G., 2003, *A&A*, 401, 1087
- Baglin A., 2003, *Adv. Space Res.*, 31, 2,345
- Balbus S., Hawley J., 1994, *MNRAS*, 266
- Ball W. H., Gizon L., 2014, *A&A*, 568, A123
- Ball W. H., Gizon L., 2017, *A&A*, 600, A128
- Benomar O. et al., 2013, *ApJ*, 767, 158
- Borucki W. J. et al., 2010, *Science*, 327, 977
- Cantiello M., Mankovich C., Bildsten L., Christensen-Dalsgaard J., Paxton B., 2014, *ApJ*, 788, 93
- Casagrande L., Ramirez I., Melendez J., Bessell M., Asplund M., 2010, *A&A*, 512, A54
- Ceillier T., Eggenberger P., García R. A., Mathis S., 2013, *A&A*, 555, A54
- Charbonnel C., Talon S., 2005, *Science*, 309, 2189
- Christensen-Dalsgaard J., 2008, *Astrophys. Space Sci.*, 316, 113
- Deheuvels S. et al., 2014, *A&A*, 564, A27
- Deheuvels S., Ballot J., Beck P. G., Mosser B., Østensen R., García R. A., Goupil M. J., 2015, *A&A*, 580, A96

- Deheuvels S., Ballot J., Eggenberger P., Spada F., Noll A., Hartogh J. W. d., 2020, *A&A*, 641, A117
- Di Mauro M. P., Ventura R., Corsaro E., Moura B. L. D., 2018, *ApJ*, 862, 9
- Eggenberger P., Montalbán J., Miglio A., 2012, *A&A*, 544, L4
- Eggenberger P. et al., 2019, *A&A*, 621, A66
- Fellay L., Buldgen G., Eggenberger P., Khan S., Salmon S. J. A. J., Miglio A., Montalbán J., 2021, *A&A*, 654, A133
- Fuller J., Cantiello M., Stello D., García R. A., Bildsten L., 2015, *Science*, 350, 423
- Garaud P., 2002, *MNRAS*, 335, 707
- García R. A. et al., 2014, *A&A*, 572, A34
- Gehan C., Mosser B., Michel E., Samadi R., Kallinger T., 2018, *A&A*, 616, A24
- Gough D. O., 2015, *Space Sci. Rev.*, 196, 15
- Gough D. O., Thompson M. J., 1990, *MNRAS*, 242, 25
- Heger A., 1998, PhD thesis, Technical University of Munich
- Hermes J. J., Kawaler S. D., Bischoff-Kim A., Provencal J. L., Dunlap B. H., Clemens J. C., 2017, *ApJ*, 835, 277
- Hoffman M. D., Gelman A., 2011, arXiv e-prints, [arXiv:1111.4246](https://arxiv.org/abs/1111.4246)
- Kissin Y., Thompson C., 2015, *ApJ*, 808, 35
- Li Y., Bedding T. R., Li T., Bi S., Stello D., Zhou Y., White T. R., 2020, *MNRAS*, 495, 2363
- Maeder A., Meynet G., 2000, *Ann. Rev. Astron. Astrophys.*, 38, 143
- Marques J. P. et al., 2013, *A&A*, 549, A74
- McQuillan A., Mazeh T., Aigrain S., 2014, *ApJS*, 211, 24
- Menou K., Mer J. L., 2006, *ApJ*, 650, 1208
- Noll A., Deheuvels S., Ballot J., 2021, A187 *A&A*, 647
- Ouazzani R.-M., Marques J. P., Goupil M.-J., Christophe S., Antoci V., Salmon S. J. A. J., 2019, *A&A*, 626, A121
- Paxton B., Bildsten L., Dotter A., Herwig F., Lesaffre P., Timmes F., 2010, *ApJS*, 192, 3
- Paxton B. et al., 2013, *ApJS*, 208, 4
- Paxton B. et al., 2015, *ApJS*, 220, 15
- Paxton B. et al., 2019, *ApJS*, 243, 10
- Pinçon C., Belkacem K., Goupil M. J., Marques J. P., 2017, *A&A*, 605, A31
- Salvatier J., Wiecki T. V., Fonnesbeck C., 2016, *PeerJ Comput. Sci.*, 2, e55
- Santos A. R. G., Breton S. N., Mathur S., García R. A., 2021, *ApJS*, 255, 17
- Schunker H., Schou J., Ball W. H., 2016, *A&A*, 586, A24
- Spada F., Gellert M., Arlt R., Deheuvels S., 2016, *A&A*, 589, A23
- Strugarek A., Brun S., Zahn J., 2011, *A&A*, 532, A34
- Takahashi K., Langer N., 2021, *A&A*, 646, A19
- Unno W., Osaki Y., Ando H., Saio H., Shibahashi H., 1989, Nonradial Oscillations of Stars, <https://ui.adsabs.harvard.edu/abs/1989nos..book.....U>

APPENDIX A: SAMPLING RESULTS

Here, we provide the posteriors following sampling of each set of rotational splittings.

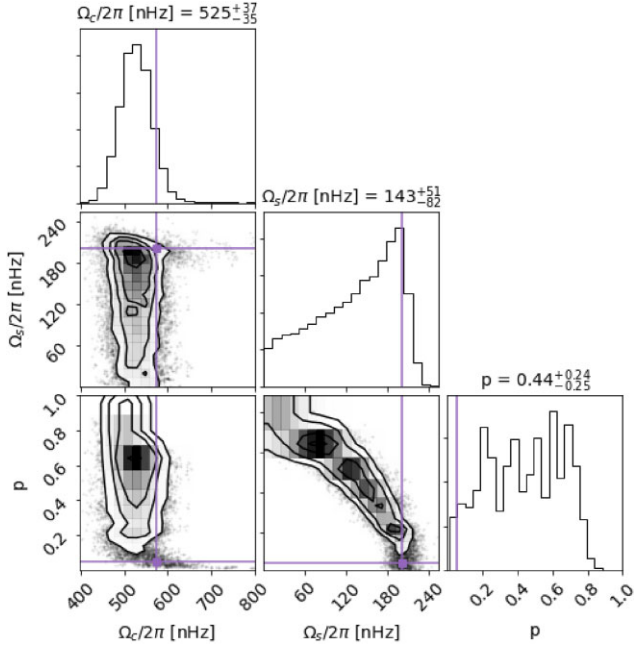


Figure A1. Posterior distributions using mock data generated with a step function aligned with the H burning shell ($r/R = 0.05$, purple profile in Fig. 2). True values are indicated in purple. There is considerable multimodality and degeneracy present.

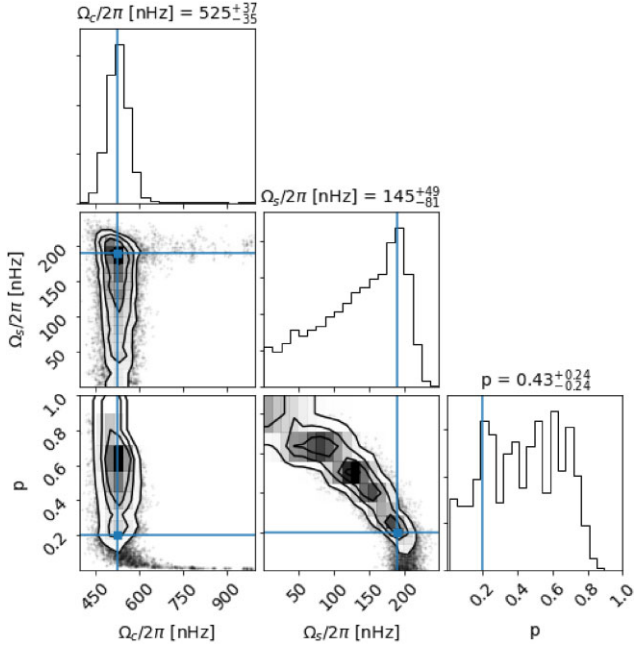


Figure A2. Posterior distributions using mock data generated with a step function in the radiative region ($r/R = 0.2$, blue profile in Fig. 2) and realistic uncertainties. True values in blue.

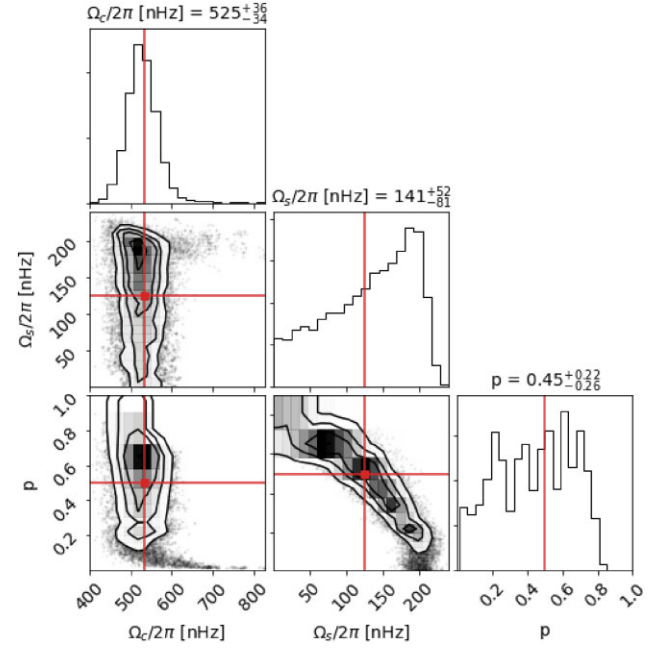


Figure A3. Posterior distributions using mock data generated with a step function at the BCZ ($r/R = 0.5$; red profile in Fig. 2), and realistic uncertainties. True values in red.

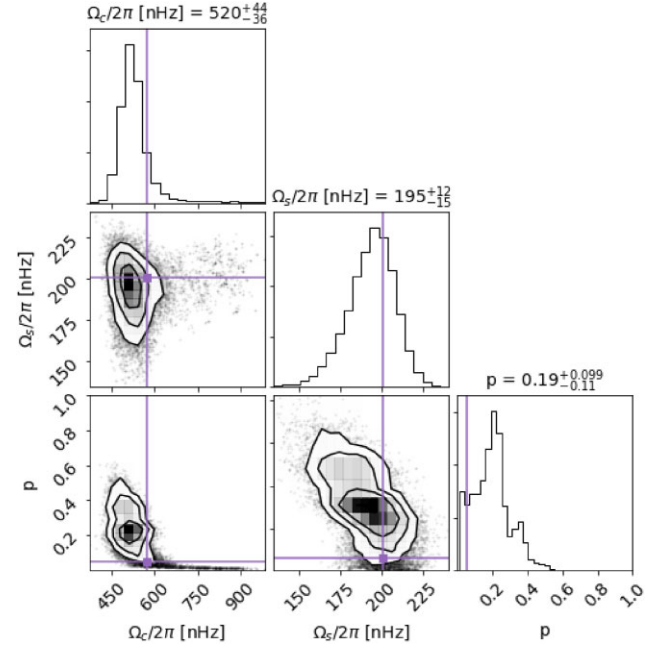


Figure A4. Posterior distributions using mock data generated with a step profile at the g-mode cavity ($r/R = 0.05$; purple profile in Fig. 2), with realistic uncertainties, and a 10 per cent prior on surface rotation Ω_s . There is still degeneracy between p and the rotation parameters (e.g. Fig. A1), but the prior has collapsed all other modes.

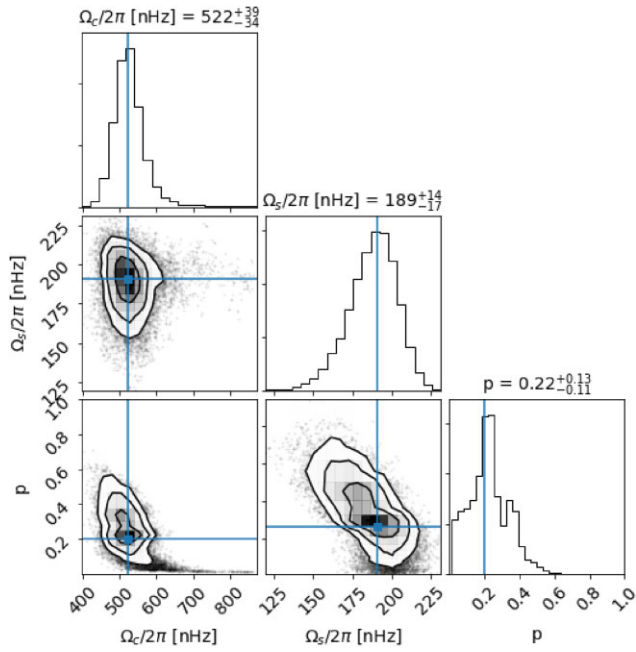


Figure A5. Posterior distributions using mock data generated with a step profile in the radiative region ($r/R = 0.20$; blue profile in Fig. 2), with realistic uncertainties, and a 10 per cent prior on surface rotation Ω_s (compare with Fig. A2).

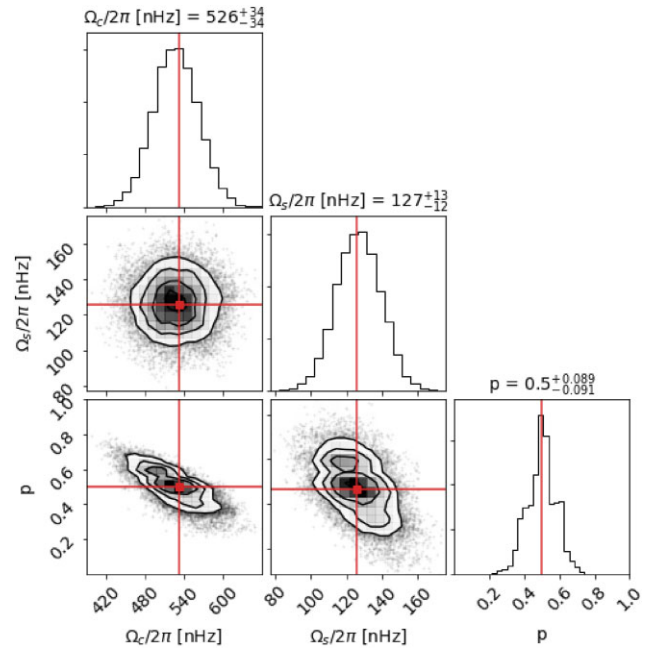


Figure A6. Posterior distributions using mock data generated with a step profile at the BCZ ($r/R = 0.50$; red profile in Fig. 2), with realistic uncertainties, and a 10 per cent prior on surface rotation Ω_s (compare with Fig. A3).

This paper has been typeset from a \LaTeX file prepared by the author.